Article

Stimulated Raman Scattering in Alkali-Earth Tungstate and Molybdate Crystals at Both Stretching and Bending Raman Modes under Synchronous Picosecond Pumping with Multiple Pulse Shortening Down to 1 ps

Milan Frank [1],* , Sergei N. Smetanin [1], Michal Jelínek [1], David Vyhlídal [1], Vladislav E. Shukshin [2], Lyudmila I. Ivleva [2], Elizaveta E. Dunaeva [2], Irina S. Voronina [2], Petr G. Zverev [2] and Václav Kubeček [1]

[1] Faculty of Nuclear Sciences and Physical Engineering, Czech Technical University, Břehová 7, 11519 Prague 1, Czech Republic; ssmetanin@bk.ru (S.N.S.); michal.jelinek@fjfi.cvut.cz (M.J.); david.vyhlidal@fjfi.cvut.cz (D.V.); vaclav.kubecek@fjfi.cvut.cz (V.K.)

[2] Prokhorov General Physics Institute of the Russian Academy of Sciences, Vavilova 38, 119991 Moscow, Russian; shukshinve@lst.gpi.ru (V.E.S.); ivleva@lst.gpi.ru (L.I.I.); edynaeva@rambler.ru (E.E.D.); irina.voronina.78@list.ru (I.S.V.); zverev@lst.gpi.ru (P.G.Z.)

* Correspondence: frankmil@fjfi.cvut.cz; Tel.: +420-224-358671

Abstract: Comparative investigation of characteristics of spontaneous and stimulated Raman scattering (SRS) in different alkali-earth tungstate and molybdate crystals at both high and low frequency anionic group vibrations is presented. It has been found that, among these crystals, the $SrMoO_4$ and $SrWO_4$ crystals are the most perspective for SRS generation on both stretching and bending modes of internal anionic group vibrations with the strongest SRS pulse shortening under synchronous laser pumping because of not only highly intense stretching mode Raman line for efficient primary extra cavity long-shifted SRS conversion but also the widest bending mode Raman line for the strongest SRS pulse shortening down to the inverse width of the widest Raman line (~1 ps) at secondary intracavity short-shifted SRS conversion. The strongest 26-fold pump pulse shortening down to 1.4 ps at the Stokes component with the combined Raman shift in the synchronously pumped extra cavity $SrMoO_4$ and $SrWO_4$ Raman lasers has been demonstrated. It was found that synchronously pumped cascade SRS with combined Raman shift is more efficient in the $SrWO_4$ crystal because the bending mode Raman line is more intense relative to the stretching mode Raman line than that in $SrMoO_4$.

Keywords: alkali-earth tungstate; molybdate crystals; stretching; bending Raman modes; stimulated Raman scattering

1. Introduction

Alkali-earth tungstate and molybdate crystals belonging to a scheelite family were proposed as the most efficient active materials for stimulated Raman scattering (SRS) [1–3]. To date, such crystals were widely used in a great number of crystalline Raman lasers where the most intense Raman mode with the highest wavenumber of $\nu_1 \sim 879$–925 cm^{-1} corresponding to totally symmetric stretching internal vibration of the crystal anionic group was utilized [4–38]. These crystals can also be doped with rare-earth ions of Nd^{3+}, Er^{3+}, Tm^{3+} and Ho^{3+} [39–53] to combine lasing and SRS properties in one active crystal for compact self-Raman laser operation in contrast to the most popular CVD-diamond [54,55] and $Ba(NO_3)_2$ [56,57] crystals which have an advantage of the highest Raman

gain but cannot be activated by laser-ion doping. One more interesting property of the scheelite-type tungstate and molybdate crystals is the presence of two intense vibrational lines in their spontaneous Raman spectra: the most intense one corresponds to the above mentioned high-wavenumber (ν_1) stretching mode (A_g) but the second line has a low wavenumber of about $\nu_2 \sim 324–336$ cm^{-1} and is the widest due to an overlap of two symmetric bending modes ($A_g + B_g$) of internal vibrations of the crystal anionic group [58]. In contrast to the single-pass SRS lasing in such crystals taking place only on the most intense ν_1 Raman mode [4–6,9,11,35,39], utilization of the optical cavity for the Raman-active crystal can also stimulate the SRS lasing with the ν_2 Raman shift. For the first time, it was demonstrated in reference [59] using a BaWO$_4$ crystal ($\nu_1 = 925$ cm^{-1}, $\nu_2 = 332$ cm^{-1}) having the most intense ν_1 and ν_2 Raman lines among the alkali-earth tungstate and molybdate crystals because the Raman lines in BaWO$_4$ are the narrowest due to the highest size and mass of the Ba^{2+} cation in the row Ca^{2+}→Sr^{2+}→Ba^{2+} [2,3,5]. The SRS generation was obtained in the extra cavity BaWO$_4$ Raman laser with not only the primary ν_1 shift but also with the secondary ν_2 shift under nanosecond laser pumping at wavelengths of 0.53 μm [59] and 1.34 μm [60]. Later, single ν_2-shifted SRS generation [61,62] and competition of the ν_1 and ν_2 lines [63,64] in BaWO$_4$ Raman lasers with intracavity nanosecond pumping at the wavelength of 1.06 μm were reported. Note that the bending-mode ν_2 Raman line is several times wider than the stretching-mode ν_1 Raman line. This property of the ν_2 line has an importance for the transient regime of SRS but the ν_2-shifted SRS radiation was generated in a quasi-steady-state regime [59–64].

Realization of transient SRS can help to strongly shorten the SRS pulse in comparison with the pump pulse. In the case of a transient single-pass SRS, the possibility of the radiation temporal shape control appears due to a delay of generating SRS pulse because the transient SRS gain depends on the pumping energy density and not the pumping intensity [65] in contrast to the quasi-steady-state SRS. However, picosecond pulse shortening at single-pass (ν_1-shifted) SRS in crystals [6,10,11,35] was weak (about 2 times). A more interesting method of pulse shortening in transient SRS is using the intracavity SRS that was theoretically predicted in work [66]. Such pulse shortening effect can be very strong because the SRS pulse should be shortened down to the inverse width of the spontaneous Raman spectrum line under intracavity mode-locked laser pumping that has a similar nature with ultra-short pulse formation in mode-locked lasers. The method was experimentally confirmed in different schemes of intracavity crystalline Raman lasers generating the first Stokes component [67,68] but lasing efficiency was low because of difficulty to make stable and efficient both fundamental and SRS mode-locked lasing in one common laser cavity. Another possible method of SRS pulse shortening is using the extra cavity synchronously-pumped mode-locked Raman laser which can be highly efficient. The SRS generation in such crystalline Raman laser takes place under pumping by a train of ultra-short laser pulses with a repetition period synchronized with a round-trip time of the Raman laser external cavity that was realized for the first time in a LiIO$_3$ crystal in work [69], where the possibility of SRS pulse shortening by several times using the Raman laser cavity length detuning have been shown. Such pulse shortening effect is produced by a combination of group velocity walk-off and strong pump pulse depletion [70]. In recent years, this method was tested on many SRS-active crystals such as CVD-diamond [71–76], KGd(WO$_4$)$_2$ [77–79], LiNbO$_3$ [80] and BaWO$_4$ [81,82]. As noted above, the last crystal (BaWO$_4$) has two ($\nu_1 = 925$ cm^{-1} and $\nu_2 = 332$ cm^{-1}) intense vibrational Raman lines. Consequently, for the first time, in a synchronously pumped system with the BaWO$_4$ crystal in a linear external cavity [81], picosecond SRS generation was observed as a cascade process of the primary extra cavity Raman conversion on the most intense ν_1 Raman line and the secondary intracavity Raman conversion on the widest ν_2 Raman line. By controlling the external cavity length, at the ($\nu_1 + \nu_2$)-shifted 1227-nm Stokes wavelength, the 12-fold pulse shortening down to 3 ps that is equal to the inverse width of the widest ν_2 Raman line has been achieved. This can be explained by the theory of ultra-short SRS pulse formation at intracavity pumping [66] taking into account that the highly shortened ($\nu_1 + \nu_2$)-shifted SRS pulses were intracavity pumped by the ν_1-shifted SRS pulses. Using the optimized ring external cavity configuration [82] allowed to achieve

the synchronously pumped BaWO$_4$ Raman laser operation with high efficiency (up to 39%) and high output pulse energy (up to 53 nJ) of the SRS radiation with the combined ($\nu_1 + \nu_2$) Raman shift and strong pulse shortening (down to 3 ps) increasing the output peak power up to 9.6 kW at 1227 nm which was even higher than the pump peak power (6.1 kW) at 1063 nm.

In the present work, in order to achieve stronger pulse shortening, we focus on other alkali-earth tungstate and molybdate crystals besides BaWO$_4$ having very similar vibrational structure with the intense ν_1 and ν_2 Raman lines [3]. The ν_2 line characteristics of these crystals are unknown but the ν_2 line width seems to be wider than for BaWO$_4$ having the narrowest Raman lines. Therefore, the pulse shortening effect in these crystals can be stronger. Thus, we present comparative investigation of the characteristics of spontaneous and stimulated Raman scattering in different alkali-earth tungstate and molybdate crystals at both high and low frequency anionic group vibrations. We demonstrate possibilities of the strongest 26-fold pulse shortening down to 1.4 ps at the ($\nu_1 + \nu_2$)-shifted Stokes component in the synchronously pumped extra cavity Raman lasers based on SrMoO$_4$ and SrWO$_4$ crystals.

2. Theoretical Approach

It is well-known that amplification of a Stokes SRS field under an undepleted pumping condition is described by the system of coupled equations [65]

$$
\begin{aligned}
\frac{\partial q^*(z,\tau)}{\partial \tau} + \Gamma q^*(z,\tau) &= i k_1 E_S(z,\tau) E_p^*(\tau), \\
\frac{\partial E_S(z,\tau)}{\partial z} &= -i k_2 q^*(z,\tau) E_p(\tau),
\end{aligned}
\tag{1}
$$

where k_1 and k_2 are coupling coefficients including the Raman susceptibility, E_p and E_S are the pump and Stokes optical field amplitudes, respectively, q is the vibrational field amplitude of the Raman-active medium, $\Gamma = 1/\tau_R$ is the dumping coefficient of the vibrational amplitude, $\tau_R = 1/(\pi c \Delta\nu_R)$ is the dephasing time of Raman scattering of the active vibrational mode with a linewidth (FWHM) of $\Delta\nu_R$, z is the longitudinal coordinate, $\tau = t - z/u$ is the local time, running with the group velocity of light u (the difference in the group velocities of SRS and pump radiations is neglected).

A solution of equations system (1) for quasi-steady-state SRS, if the pump pulse duration τ_p is much longer than the dephasing time τ_R, is also well-known [65]. It can be easily found if we neglect the derivative in the first equation of the system (1):

$$
|E_S(z,\tau)|^2 = |E_S(0,\tau)|^2 \exp\left(2k_1 k_2 |E_p(\tau)|^2 z/\Gamma\right) = |E_S(0,\tau)|^2 \exp\left(g I_p(\tau) z\right),
\tag{2}
$$

where g is the steady-state Raman gain coefficient (in cm/W), $I_p(\tau)$ is the pump radiation intensity (in W/cm^2), $g I_p(\tau) = 2k_1 k_2 |E_p(\tau)|^2/\Gamma$ is the steady-state Raman gain factor (in cm^{-1}). Therefore, the quasi-steady-state SRS amplification has exponential growth with the increment [65]

$$
G_0 = g I_p L,
\tag{3}
$$

where I_p is the average value of the pump radiation intensity, L is the SRS interaction length. So, the quasi-steady-state ($\tau_p \gg \tau_R$) single-pass SRS amplification is independent on the pump pulse duration τ_p.

For arbitrary duration of the pump pulse, system (1) has been integrated only partially [65,83]:

$$
E_S(z,\tau) = E_S(0,\tau) + \sqrt{k_1 k_2 z} E_p(\tau) \int\limits_{-\infty}^{\tau} \frac{E_p^*(\tau') E_S(0,\tau') e^{-\Gamma(\tau-\tau')} I_1\left(\sqrt{4 k_1 k_2 z [u(\tau) - u(\tau')]}\right)}{\sqrt{u(\tau) - u(\tau')}} d\tau',
\tag{4}
$$

where $I_1(x)$ is the modified first-order Bessel function and $u(\tau) = \int_{-\infty}^{\tau} |E_p(\tau')|^2 d\tau'$ is the pump energy parameter. The integral in expression (4) is unsolvable in general.

In the case of highly transient SRS with $\tau_p < \tau_R$, when the factor $exp[-\Gamma(\tau - \tau')]$ in expression (4) can be replaced with unity, the solution was found [84] to be

$$|E_S(z, \tau)|^2 = |E_S(0, \tau)|^2 I_0^2 \left(\sqrt{4k_1k_2zu(\tau)} \right). \tag{5}$$

Therefore, highly transient SRS gain increment G (at $\tau_p < \tau_R$) in the case of a rectangular pump pulse can be determined (at $z = L$ and $\tau = \tau_p$) as

$$G = \ln[I_0^2(\sqrt{2G_0\tau_p/\tau_R})] \approx 2\sqrt{2G_0\tau_p/\tau_R} - \ln(2\pi\sqrt{2G_0\tau_p/\tau_R}), \tag{6}$$

where we used the approximate equality assuming that the modified zero-order Bessel function is close to $I_0(x) \approx exp(x)/\sqrt{2\pi x}$ which is valid for $x > 1/4$. The second term in the approximate expression is essentially lower than the first term, so highly transient SRS amplification has growth close to exponential as for the quasi-steady-state case but the increment G Equation (6) of this growth is essentially lower than G_0 Equation (3) due to not only a square root but also $\tau_p/\tau_R < 1$. So, the SRS radiation intensity amplification at both quasi-steady-state and transient cases can be considered as $I_S = I_{S0} \cdot exp(G)$ where I_{S0} and I_S are input (or seed) and output intensities of the SRS radiation ($G \equiv G_0$ at the quasi-steady-state case). Expression (6) takes also into account that the quasi-steady-state SRS gain increment G_0 can be used as the pumping parameter even for transient SRS.

In work [85], the approximate solution, which is valid not only at highly transient case ($\tau_p < \tau_R$) but at full transient SRS condition at $\tau_p < 20\tau_R$, was found. However, this work was focused on high values of the pumping parameter G_0 (>10) to estimate single-pass transient SRS generation threshold. Therefore, the first term in the solvable integral Equation (4) was neglected.

Now, we need to estimate threshold of extra cavity transient SRS laser oscillation. The external cavity for the Raman-active medium is used to decrease the threshold value G_{0th} of the pumping parameter G_0 and it can be even lower than unity balancing with the cavity losses in spite of transient SRS. Therefore, we need to solve Equation (4) more accurately.

As in reference [85], we use the approximation based on reducing the integrand to the exponential form to make the integral in expression (4) solvable. We use now more accurate approximation based on the asymptotic form of the modified *n*-order Bessel function $I_n(x) = \left[exp(x)/\sqrt{2\pi x}\right]\left[1 - (4n^2 - 1)/8x + \cdots\right]$ taking into account two first terms, that is, for $I_1(x)$ in Equation (4) we use $I_1(x) \approx \left[exp(x)/\sqrt{2\pi x}\right][1 - 3/8x]$ which is valid for $x > 1/2$. In the obtained integrand, the coefficient at the exponent changes slowly and its dependence on the integration variable can be neglected. Instead of the Equation (4) in the case of a rectangular pump pulse, we obtain the equation for the SRS gain increment:

$$G \approx \ln\left[\left|1 + \frac{\sqrt[4]{2G_0\tau_p/\tau_R}}{\sqrt{8\pi}\tau_p}\left(1 - \frac{3}{8\sqrt{2G_0\tau_p/\tau_R}}\right)\int_0^{\tau_p} e^{-\Gamma(\tau_p-\tau')/\tau_R+\sqrt{2G_0(\tau_p-\tau')/\tau_R}}d\tau'\right|^2\right], \tag{7}$$

which is solvable. The solution is

$$G \approx \ln\left[\left|1 + \frac{\sqrt[4]{2G_0\tau_p/\tau_R}}{\sqrt{8\pi}\tau_p/\tau_R}\left(1 - \frac{3}{8\sqrt{2G_0\tau_p/\tau_R}}\right)\left\{1 - exp\left(\sqrt{2G_0\frac{\tau_p}{\tau_R}} - \frac{\tau_p}{\tau_R}\right)\right.\right.\right.$$
$$\left.\left.\left. + \sqrt{\frac{\pi G_0}{2}}\left[erf\left(\sqrt{\frac{\tau_p}{\tau_R}} - \sqrt{\frac{G_0}{2}}\right) + erf\left(\sqrt{\frac{G_0}{2}}\right)\right]exp\left(\frac{G_0}{2}\right)\right\}\right|^2\right], \tag{8}$$

which can be used for the rectangular pump pulse with arbitrary duration τ_p at $G_0\tau_p/\tau_R > 1/8$.

In the case of single-pass quasi-steady-state SRS, the criterial condition of the SRS generation threshold was determined in Reference [86] as $G_{0th} \approx 25$ corresponding to conversion of the pump radiation into the Stokes SRS component of approximately 1%. For the transient case ($\tau_p < 20\tau_R$),

a similar condition $G_{th} \approx 25$ can be used [11,85] implying that the threshold value of the pumping parameter $G_{0th} = gI_{p,th}L$ should be higher according to expressions (6) and (8).

Using the external cavity for the Raman medium allows to decrease the threshold of SRS generation but the threshold condition become dependent on τ_p even for quasi-steady-state SRS [23] because, in the optical cavity with a round-trip time τ_c, the SRS oscillation takes place as long as the τ_p-long pump pulse acts. If the SRS conversion is weak and depletion of pumping can be neglected, development of the extracavity Raman lasing at single-pass pumping can be defined by the expression [87]

$$\tau_c \frac{dI_S}{dt} = (p \cdot G - K)I_S \tag{9}$$

where $p \cdot G$ is the round-trip SRS gain increment, G is the single-pass SRS gain increment described by expression (8), $p = 1$ for a ring cavity, $p = 2$ for a linear cavity at $\tau_p > \tau_c$, $K = ln(1/T_S R_S)$ is the round-trip loss increment defined by the losses of the cavity, T_S is round-trip transmission of the intracavity medium including all intracavity losses per round-trip of the cavity (it is single-pass transmission for a ring cavity or double-pass transmission for a linear cavity), R_S is reflection of the output coupler, $\tau_c = L_c/c$ or $\tau_c = 2L_c/c$ is the round-trip time for a ring or linear cavity, respectively, L_c is an optical length of the cavity. Integrating expression (9) with respect to time from zero up to τ_p (the case of the rectangular pump pulse), we obtain

$$I_S = I_{S0} \exp[(p \cdot G - K)\tau_p/\tau_c] \tag{10}$$

and so by analogy with the single-pass SRS ($G_{th} \approx 25$), the extracavity SRS oscillation threshold became

$$(p \cdot G_{th} - K)\tau_p/\tau_c \approx 25. \tag{11}$$

Taking into account all the cavity characteristics, we obtain

$$G_{th} \approx 25\frac{\tau_c}{\tau_p p} + \frac{1}{p} \ln \frac{1}{T_S R_S} \tag{12}$$

For example, for quasi-steady-state SRS ($\tau_p \gg \tau_R$), using expression (3) we can express the threshold pump intensity [23]

$$I_{p,th} = \frac{25}{gL}\left(\frac{\tau_c}{\tau_p p} + \frac{1}{25p} \ln \frac{1}{T_S R_S}\right) \tag{13}$$

where the factor in the brackets is the cavity parameter which is lower than unity, so it decreases the threshold pump intensity $I_{p,th}$ in comparison with the single-pass SRS generation threshold of $I_{p,th} \approx 25/(gL)$. According to expression (13), decreasing the pump pulse duration τ_p in comparison with the cavity round-trip time τ_c leads to increasing the intensity $I_{p,th}$. At single pulse pumping with $\tau_p < \tau_c$, the cavity cannot help to decrease the SRS threshold, so it has the single-pass SRS threshold value $I_{p,th} \approx 25/(gL)$. Usually, the τ_c value exceeds a nanosecond and it is difficult to realize transient SRS in a cavity under pumping by a single pulse shorter than a nanosecond.

At the limit of $\tau_p \gg \tau_c$, from the expression (12), we obtain the lowest oscillation threshold condition

$$G_{th} \approx \frac{1}{p} \ln \frac{1}{T_S R_S} \tag{14}$$

usually used not only for Raman lasers but for all lasers because it presents the condition of balance between gain and losses in a laser.

Interesting possibility is opened using pumping by repetitive pulses with a repetition period synchronized with the cavity round-trip time τ_c. The individual pump pulses can be shorter than τ_c and even ultra-short realizing transient SRS in a cavity. Such systems are synchronously pumped Raman lasers [67–82]. If we use a train of ultra-short pulses with the pulse train duration of t_p at the individual pulse duration of τ_p, the extracavity synchronously pumped SRS oscillation threshold will

be defined by expression (12) where τ_p should be replaced with t_p and $p = 1$ for both ring and linear cavities (at $\tau_p < \tau_c$ we have gain only in the forward direction) but the SRS gain G (and its threshold value G_{th} in expression (12)) is defined by τ_p as before by expression (8). Using mode locking for the pump laser, it is easy to obtain a very high value of t_p (quasi-continuous-wave mode-locking) and even continuous-wave mode-locking ($t_p \to \infty$). Then, we fulfil the condition $t_p \gg \tau_c$ for the lowest SRS oscillation threshold and can apply expression (14) at $p = 1$ for estimation of oscillation threshold in extracavity synchronously pumped quasi-continuous-wave mode-locked Raman lasers.

3. Raman Crystal Characterization

Alkali-earth orthotungstate and orthomolybdate crystals (MXO_4 where M = Ca, Sr, Ba; X = W, Mo) crystallize in the tetragonal scheelite-type structure of C_{4h}^6 space symmetry. The approximation of almost free anions $(XO_4)^{2-}$ can be applied to these compounds because covalent bonds between Mo or W and four oxygen atoms are stronger than a bond between the full $(WO_4)^{2-}$ or $(MoO_4)^{2-}$ tetragonal anionic groups with the cation sublattice. This makes it possible to distinguish the so-called internal and external modes in the vibrational spectrum. The internal vibrations correspond to the oscillations inside the $(WO_4)^{2-}$ or $(MoO_4)^{2-}$ anionic groups with an immovable mass centre; the external or lattice phonons correspond to the motion of the cation and the rigid molecular unit [3]. This approximation allows to consider the most intense lines in spontaneous Raman spectrum as the anionic group internal vibrations splitting by a crystalline field. These most intense lines correspond to symmetric stretching and bending internal vibrations of anionic groups with high and low wavenumber of ν_1 and ν_2, respectively. The high wavenumber vibrational Raman mode at ν_1 is the strongest corresponding to internal totally symmetric stretching vibration ($A_g(\nu_1)$ mode) of W-O or Mo-O bond in the anionic group [58]. The secondary Raman line at ν_2 is less intense and broadened, corresponding to two overlapping modes $A_g(\nu_2) + B_g(\nu_2)$ of symmetric bending of O-W-O or O-Mo-O bond [58]. The high wavenumber (ν_1) Raman mode characteristics of alkali-earth tungstate and molybdate crystals were studied in Reference [1–3]. It was found [3] that, for these crystals, excluding scheelite $CaWO_4$, values of the ν_1 Raman line peak intensity (i.e., peak Raman scattering cross-section) are almost as large as in a $Ba(NO_3)_2$ crystal but values of integral Raman scattering cross-section at ν_1 (which is determined by the ν_1 Raman line peak intensity multiplied by its width $\Delta\nu_1$) are 2.5–3 times higher than for $Ba(NO_3)_2$ and only 1.6–2 times lower than for diamond (barium nitrate and diamond are the most popular Raman-active crystals having the highest Raman gain). Therefore, alkali-earth tungstate and molybdate crystals are the most perspective for both quasi-steady-state and transient regimes of SRS as well as diamond but they also have the secondary (ν_2) Raman line in comparison with diamond.

In order to study the ν_2 Raman line characteristics and compare them with the ν_1, we measured polarized spontaneous Raman scattering spectra of all alkali-earth tungstate and molybdate crystals with high spectral resolution. We used double monochromator "*SPEX-Ramalog 1403*" with the excitation by a 510.6-nm copper vapor laser with the spectral resolution of 0.5 cm^{-1} and scanning step of 0.2 cm^{-1}.

Both the ν_1 and ν_2 lines in spontaneous Raman spectrum of alkali-earth tungstate and molybdate crystals are the most intense when the exciting light is linearly polarized along the crystal optical axis, that is, in the **E**∥c orientation. The comparative data measured for this orientation are presented in Table 1.

Values of the width $\Delta\nu_2$ of the ν_2 Raman line, its peak intensity I_2 and the ratio I_1/I_2 of peak intensities of the ν_1 and ν_2 lines are the most important data for us here because we realize cascade SRS firstly on the most intense ν_1 line and secondly on the widest ν_2 line for the benefit of the strongest pulse shortening down to the inverse value of the widest linewidth $\Delta\nu_2$.

The ν_2 line of the bending vibration for the $(WO_4)^{2-}$ and $(MoO_4)^{2-}$ anionic groups is slightly shifted along the tungstate (ν_2 = 332–336 cm^{-1}) and molybdate (ν_2 = 322–327 cm^{-1}) series, which is the same way as for the ν_1 line of the stretching vibration for the tungstate (ν_1 = 910–925 cm^{-1}) and molybdate (ν_1 = 879–892 cm^{-1}) series. The ν_2 wavenumber in the molybdates is lower because the

unit cell is larger. Due to the overlap of two bending modes [$A_g(\nu_2)$ + $B_g(\nu_2)$], the linewidth $\Delta\nu_2$ is essentially (2–4 times) wider than the linewidth $\Delta\nu_1$ except for $CaWO_4$ and $CaMoO_4$ having the highly broadened ν_1 line.

Table 1. Spontaneous Raman scattering parameters of alkali-earth tungstate and molybdate crystals in **E**∥*c* orientation.

Crystal	ν_1, cm^{-1}	$\Delta\nu_1$, cm^{-1}	I_1, *	ν_2, cm^{-1}	$\Delta\nu_2$, cm^{-1}	I_2, *	I_1/I_2
$CaWO_4$	910	6.9	18	334	9	10	1.8
$SrWO_4$	921	2.7	41	336	8.7	12	3.5
$BaWO_4$	925	1.6	64	332	3.8	27	2.4
$CaMoO_4$	879	5.5	34	322	8	17	2
$SrMoO_4$	888	2.6	51	327	10.5	11	4.8
$BaMoO_4$	892	2.1	62	324	4	31	2

* Values of the Raman line peak intensities $I_{1,2}$ are presented in % with respect to the line peak intensity of the Raman-active mode (1333 cm^{-1}) of diamond with an equal length.

In all the crystals, there is a correlation between the values $I_{1,2}$ and $\Delta\nu_{1,2}$ because an increase in the line intensities $I_{1,2}$ takes place due to an increase in the phase relaxation (dephasing) time $\tau_{1,2} = 1/\pi c\Delta\nu_{1,2}$ at approximately equal values of the integral Raman scattering cross-section ($I_{1,2}\cdot\Delta\nu_{1,2}$). The intensity I_1 of the high wavenumber line and its phase relaxation time $\tau_1 = 1/\pi\,c\Delta\nu_1$ have smooth increasing with cation replacement in the row $Ca^{2+}\rightarrow Sr^{2+}\rightarrow Ba^{2+}$ for each anionic group. On the other hand, the low wavenumber line intensity I_2 and its phase relaxation time $\tau_2 = 1/\pi c\Delta\nu_2$ change only slightly with cation replacement $Ca^{2+}\rightarrow Sr^{2+}$ but I_2 and τ_2 increase significantly (more than 2 times) for Ba^{2+}. This anomalous property of the ν_2 Raman line can be caused by the same factors as its anomalously low difference in wavenumbers ν_2 with cation replacement $Ca^{2+}\rightarrow Sr^{2+}\rightarrow Ba^{2+}$ for each anionic group. It can be explained by compensation (for the ν_2 Raman line) between the influence of growing mass and size of the cation with the influence of the Davydov splitting effect [3]. If the first is predominant for lower ($<\nu_2$) wavenumber external vibrations decreasing the vibrational level energy with cation replacement $Ca^{2+}\rightarrow Sr^{2+}\rightarrow Ba^{2+}$ (in this row the cation mass and size increase), the second is predominant for the highest (ν_1) wavenumber internal vibrations increasing the vibrational level energy in the row $Ca^{2+}\rightarrow Sr^{2+}\rightarrow Ba^{2+}$ [3]. As a result, the $SrWO_4$ and $SrMoO_4$ crystals have the widest ν_2 Raman lines as in $CaWO_4$ and $CaMoO_4$ and also have the highly intense ν_1 Raman lines as in $BaWO_4$ and $BaMoO_4$. Hence, $SrWO_4$ and $SrMoO_4$ crystals are the most perspective having not only high Raman gain coefficients of *g* = 4.7 and 5.6 cm/GW at 1.06-μm pumping [11] (*g* is proportional to I_1) but also the widest ν_2 Raman lines ($\Delta\nu_2$ = 8.7 cm^{-1} and 10.5 cm^{-1}, respectively) allowing to obtain SRS pulse shortening down to $1/\pi c\Delta\nu_2 \approx 1ps$.

For comparison of the perspective crystals, we also need to take into account the ratio I_1/I_2 of peak intensities of the ν_1 and ν_2 lines. Figure 1 shows the high resolution polarized spontaneous Raman scattering spectra of the vicinities of the ν_1 and ν_2 lines in $BaWO_4$, $SrWO_4$ and $SrMoO_4$ crystals at exciting light polarization parallel (**E**∥*c*) and perpendicular (**E**⊥*c*) to the crystal optical axis.

It can be seen that in the $BaWO_4$ crystal, having the narrowest ν_1 and ν_2 Raman lines, the ν_2 line is the most intense relative to the ν_1 line (Figure 1a), that is, the ratio I_1/I_2 = 2.4 is the lowest. In the $SrWO_4$ crystal, the ν_2 line is wider that resulted in its lower intensity relative to the ν_1 line (Figure 1b) and so the ratio is intermediate I_1/I_2 = 3.5. And the lowest intense ν_2 line relative to the ν_1 line is in the $SrMoO_4$ crystal (Figure 1c) because the ν_2 line is the widest at approximately equal widths of the ν_1 line in $SrMoO_4$ and $SrWO_4$ and so the ratio is the highest I_1/I_2 = 4.8.

Thus, we can compare characteristics of the most perspective $SrMoO_4$ and $SrWO_4$ crystals having the widest ν_2 line ($\Delta\nu_2$ ~ 10 cm^{-1}) for SRS pulse compression down to $1/\pi\,c\Delta\nu_2 \approx 1\,ps$ at cascade ($\nu_1 + \nu_2$)-shifted SRS conversion. The $SrMoO_4$ crystal has a higher intense ν_1 line giving a higher Raman gain of 5.6 cm/GW at 1.06-μm pumping which is advantageous for the primary SRS conversion on the ν_1 Raman line. However, the relative intensity of the ν_2 line in this crystal is the lowest (the ν_2 line

intensity is 4.8 times lower than the ν_1 line intensity) which is disadvantageous for the secondary SRS conversion on the ν_2 Raman line. Contrariwise, the SrWO$_4$ crystal has a lower intense ν_1 Raman line giving a lower Raman gain of 4.7 cm/GW at 1.06-µm pumping increasing the SRS oscillation threshold on the ν_1 Raman line but the relative intensity of the ν_2 line in this crystal is high (the ν_2 line intensity is only 3.5 times lower than the ν_1 line intensity) which is advantageous for the secondary SRS conversion on the ν_2 Raman line. So, synchronously pumped cascade Raman laser oscillation in SrMoO$_4$ and SrWO$_4$ requires comparison at equal conditions. Such oscillation has been recently tested [81,82] for the BaWO$_4$ crystal having the highest Raman gain of 8.5 cm/GW at 1.06-µm pumping [5] and the lowest $I_1/I_2 = 2.4$ but the narrowest $\Delta\nu_2 = 3.8$ cm^{-1}. The possibilities of efficient cascade $(\nu_1 + \nu_2)$-shifted SRS conversion (up to 39%) and strong SRS pulse shortening down to the inverse width of the ν_2 Raman line ($1/\pi c\Delta\nu_2 = 3$ ps) in BaWO$_4$ were demonstrated [82]. The cascade $(\nu_1 + \nu_2)$-shifted SRS generation in SrMoO4 was also obtained [88].
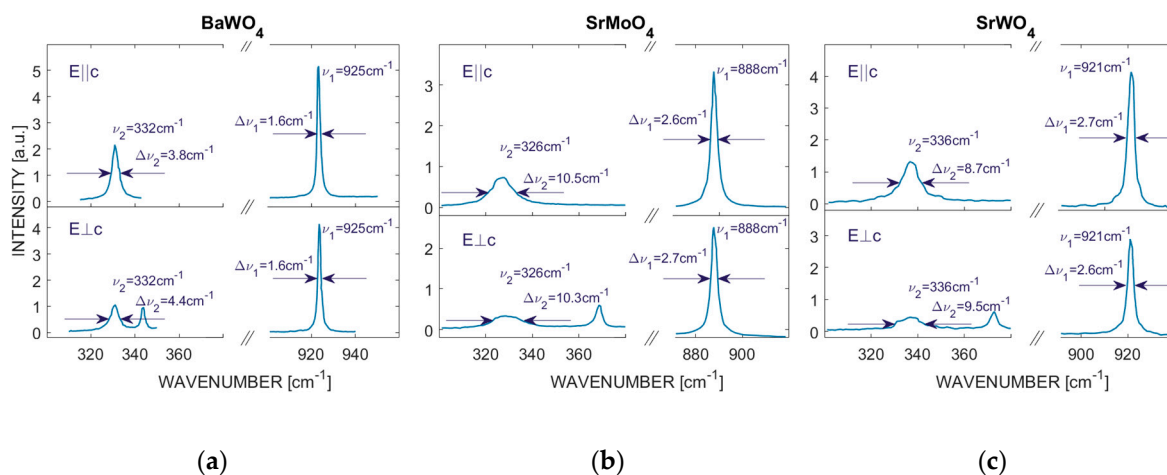

Figure 1. Polarized spontaneous Raman scattering spectra of the vicinities of the ν_1 and ν_2 lines in BaWO$_4$ (**a**), SrMoO$_4$ (**b**) and SrWO$_4$ (**c**) crystals at exciting light polarization parallel ($\mathbf{E}\|c$) and perpendicular ($\mathbf{E}\perp c$) to the crystal optical axis.

4. Experimental Setup of the Synchronously Pumped Crystalline Raman Laser

The experimental setup of the synchronously pumped Raman laser system is shown in Figure 2. The laser system is the same as used for the BaWO$_4$ and SrMoO$_4$ crystal in the previous experiments [82,88]. The *a*-cut SrMoO$_4$ and SrWO$_4$ crystals were used as the Raman-active medium. Both crystals were grown by Czochralski technique at Prokhorov General Physics Institute of the Russian Academy of Sciences. The SrMoO$_4$ crystal had a shape of a Brewster-cut slab with the length of 17 mm and cross-section of 7×5 mm^2. The SrWO$_4$ crystal was also Brewster-cut with the length of 14 mm and cross-section of 10×7 mm^2. The crystal optical axis (*c*) was oriented horizontally for pumping by $\mathbf{E}\|c$ enabling to access the maximum intensities of the ν_1 and ν_2 Raman lines (Figure 1) and the minimum losses at the Brewster incidence.

As a source for synchronously pumped Raman laser, a laboratory-designed master oscillator power amplifier (MOPA) Nd:GdVO$_4$ laser system was used. The oscillator and amplifier were based on similar Nd:GdVO$_4$ slab crystal with the dimensions of $16 \times 4 \times 2$ mm^3 in the bounce geometry. The master oscillator lasing at the wavelength of $\lambda_p = 1063$ nm generated in the continuously mode-locked regime using a semiconductor saturable absorber mirror (SESAM) with the modulation depth of 2% and non-saturable losses <2% [89]. The output continuous-wave train, consisting of 36 ps pulses at the repetition rate of 150 MHz, was amplified in the single-pass amplifier. This amplifier was pumped by a quasi-continuous (QCW) laser diode with the pulse duration of 500 µs at the repetition rate of 50 Hz. The QCW amplification of continuous wave mode-locked train was used to obtain long trains ($t_p = 500$µs) consisting of more than 70,000 picosecond pulses with smoothly varying intensity

because the amplitude and temporal stability is crucial for the stable SRS generation. The energy of a single amplified pulse was up to 221 nJ.
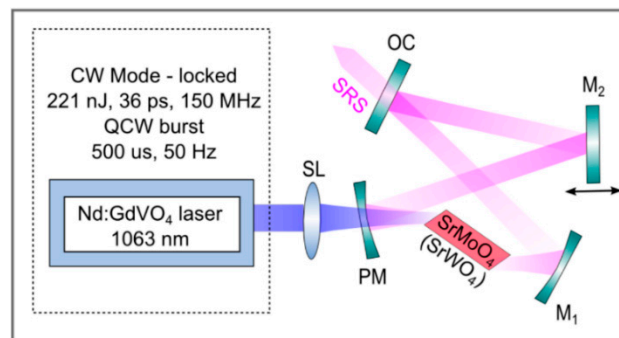

Figure 2. Experimental setup of synchronously pumped extra cavity crystalline Raman laser.

The linearly-polarized pumping radiation with the beam spatial profile close to the fundamental transversal mode was focused into a Raman crystal centre with the spot radius of 35×30 μm^2 by an anti-reflection coated spherical lens SL with the focal length of 100 mm.

The external bow tie cavity for investigated Raman laser system consisted of two concave and two flat mirrors. The concave mirrors PM, which was used at a pumping mirror and M1 had the same curvature radius of 100 mm. Two OCs (OC1 and OC2) with different reflectivities were tested for generation with single (ν_1) and combined ($\nu_1 + \nu_2$) Raman shifts. The mirror reflectivities are summarized in Table 2. Note, that the Raman cavity was designed to compensate astigmatism.

Table 2. Raman laser cavity mirrors reflectivities at pumping and Stokes wavelengths.

Mirror	R [%] 1063 nm	R [%] 1174/1178 nm	R [%] 1220/1227 nm	R [%] 1271/1279 nm	R [%] 1310/1321 nm
PM	1.3	98.9/98.9	99.4/99.4	98.1/97.1	73.6/34.0
M1	99.6	99.6/99.6	99.6/99.6	99.6/99.6	98.8/98.6
M2	99.8	99.9/99.9	99.8/99.8	99.5/99.3	89.4/47.0
OC1	99.6	87.4/88.7	85.1/80.1	51.5/68.9	66.7/63.3
OC2	99.8	99.9/99.4	96.1/96.3	78.6/66.1	23.3/16.0

For separation of individual generated Stokes components and pumping radiation, the long pass filters Thorlabs FEL1150, 1200, 1250 and 1300 (cut-on wavelength of 1150, 1200, 1250 and 1300 nm, respectively) were used. The generated SRS spectra were recorded by a spectrometer OceanOptics NIR512 operating in a wavelength range 850–1700 nm with a FWHM resolution of ~3 nm. The SRS output pulse energy was measured by a power detector Standa 11PMK-15S-H5. For determination of SRS pulse duration, the pulses were measured by a laboratory designed non-collinear second harmonic generation (SHG) autocorrelator based on a LiIO$_3$ crystal. Note that we assumed a Gaussian shape of the measured autocorrelation curves.

5. Experimental Results of SRS Lasing

The synchronously pumped SRS generation was successfully achieved in all tested crystals. The case of perfect synchronization corresponded to the lowest SRS generation threshold and the highest SRS radiation output energy. The SRS radiation in the ring cavity Raman laser was generated only in the forward direction because SRS oscillation threshold for the backscattering was essentially higher due to pumping by shorter pulse than the Raman-active crystal transit time [90].

Figure 3 demonstrates a comparison of the output SRS spectra for the 8-cm long BaWO$_4$ crystal studied earlier [82], for the 1.7-cm long SrMoO$_4$ [88] and 1.4-cm long SrWO$_4$ crystals studied here in the same configuration of the Raman laser without selective filtering of strong SRS components.
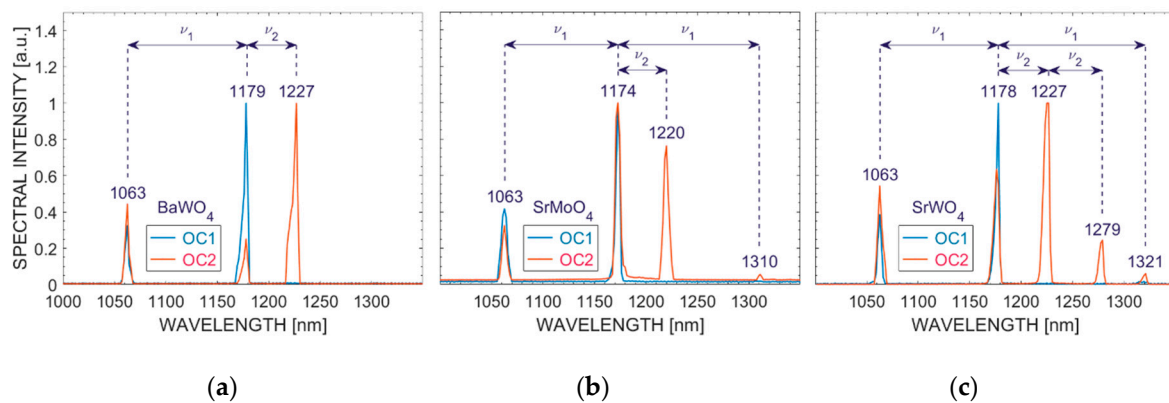
Figure 3. Output stimulated Raman scattering (SRS) radiation spectra for (**a**) BaWO$_4$ [82], (**b**) SrMoO$_4$ [88] and (**c**) SrWO$_4$ Raman lasers using two output couplers OC1 and OC2.

In the setup with the output coupler OC1, only the first Stokes components at the wavelength of 1179, 1174 and 1178 nm corresponding to Raman shift of ν_1 = 925,888 and 921 cm^{-1}, were generated in BaWO$_4$, SrMoO$_4$ and SrWO$_4$, respectively (Figure 3, blue line). In the setup with the output coupler OC2, due to lower optical losses of the output coupler OC2 at 1174–1179 nm and 1220–1279 nm, the intracavity intensity of the ν_1-shifted first Stokes SRS components were higher, so the additional Stokes components at the wavelength of 1227, 1220 and 1227 nm in BaWO$_4$, SrMoO$_4$ and SrWO$_4$, respectively, with a short wavenumber shift of ν_2 (332, 327 and 336 cm^{-1}) from the ν_1-shifted first Stokes component were also generated (Figure 3, red line).

Due to high intracavity intensity at the ν_1 long-shifted first Stokes component, the $2\nu_1$ long-shifted second Stokes component at 1310 and 1321 nm in SrMoO$_4$ and SrWO$_4$, respectively, was also generated (Figure 3b,c) but it was weak because the output coupler OC2 had low reflectivity of 23–16% at 1310–1321 nm and even lower (13%) at 1323 nm preventing the 1323-nm $2\nu_1$-shifted SRS oscillation in BaWO$_4$ [82]. The 1323-nm $2\nu_1$-shifted SRS component in the synchronously pumped Raman laser based on the same (8-cm long) BaWO$_4$ crystal was efficiently generated in work [81] using higher reflectivity (>50%) output couplers at 1323 nm.

We can also see in Figure 3c one more additional Stokes component at 1279 nm oscillating only in SrWO$_4$. It was identified as the $2\nu_2$-shifted Stokes component from the ν_1-shifted Stokes component. In comparison with SrMoO$_4$, the generation of this ($\nu_1 + \nu_2 + \nu_2$) higher order Stokes component in SrWO$_4$ can be explained by that the vibrational ν_2 Raman line has higher intensity relative to the vibrational ν_1 Raman line in SrWO$_4$ (I_1/I_2 = 3.5, see Table 1) than in SrMoO$_4$ (I_1/I_2 = 4.8, see Table 1).

Figure 4 demonstrates the Raman laser radiation spectrum for the same 1.4 cm long SrWO$_4$ crystal at the output coupler OC2 using selective filtering of the strongest (1063, 1178 and 1227 nm) radiation components for registration of all weak SRS radiation components. We can see many additional SRS components with single ($+\nu_2$) and double ($+2\nu_2$) short Stokes shifts and even single ($-\nu_2$) short anti-Stokes shift from the single ($+\nu_1$) and double ($+2\nu_1$) long-shifted Stokes components.

All SRS radiation wavelengths possible in BaWO$_4$, SrWO$_4$ and SrMoO$_4$ crystals at 1063-nm pumping are calculated in Table 3 where the experimentally realized SRS oscillation wavelengths are marked by asterisks.

If many additional short-shifted SRS components were generated in SrWO$_4$ because of the relatively intense vibrational ν_2 Raman line (I_1/I_2 = 3.5, Table 1), it is strange that it was not generated in BaWO$_4$ having more intense ν_2 Raman line in comparison with the ν_1 Raman line (I_1/I_2 = 2.4, Table 1). It can be caused by difference of the crystal lengths. The SrWO$_4$ crystal was the shortest (1.4 cm) and the BaWO$_4$ crystal was the longest (8 cm). To verify that, we prepared a long SrWO$_4$ sample and tested it in an additional experiment in the same Raman laser setup. This Brewster-cut SrWO$_4$ crystal had a length of 3.6 cm. The output SRS radiation spectra are presented in Figure 5.
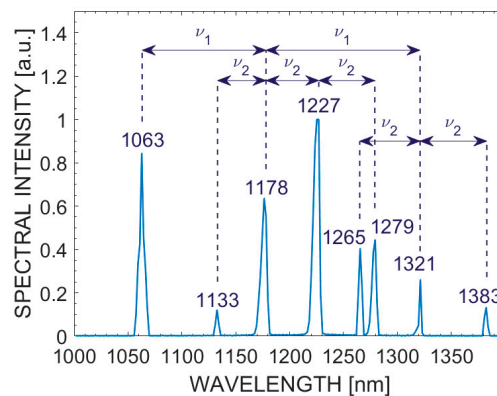
Figure 4. Registered weak SRS radiation spectral components for the short (1.4 cm) SrWO$_4$ crystal using OC2.

Table 3. SRS radiation wavelengths in BaWO$_4$, SrWO$_4$ and SrMoO$_4$ crystals at 1063-nm pumping.

SRS Radiation Wavelength	BaWO$_4$	SrMoO$_4$	SrWO$_4$
$\lambda_{1-2} = [\lambda_p{}^{-1} - (\nu_1 - \nu_2)]^{-1}$	1135 nm	1130 nm	1133 nm **
$\lambda_1 = [\lambda_p{}^{-1} - (\nu_1)]^{-1}$	1179 nm *	1174 nm *	1178 nm *
$\lambda_{1+2} = [\lambda_p{}^{-1} - (\nu_1 + \nu_2)]^{-1}$	1227 nm *	1220 nm *	1227 nm *
$\lambda_{1+1-2} = [\lambda_p{}^{-1} - (\nu_1 + \nu_1 - \nu_2)]^{-1}$	1268 nm	1256 nm	1265 nm **
$\lambda_{1+2+2} = [\lambda_p{}^{-1} - (\nu_1 + \nu_2 + \nu_2)]^{-1}$	1279 nm	1271 nm	1279 nm *
$\lambda_{1+1} = [\lambda_p{}^{-1} - (\nu_1 + \nu_1)]^{-1}$	1323 nm *	1310 nm *	1321 nm *
$\lambda_{1+1+2} = [\lambda_p{}^{-1} - (\nu_1 + \nu_1 + \nu_2)]^{-1}$	1383 nm	1369 nm	1383 nm **

* experimentally realized with considerable conversion, ** experimentally realized with weak conversion.
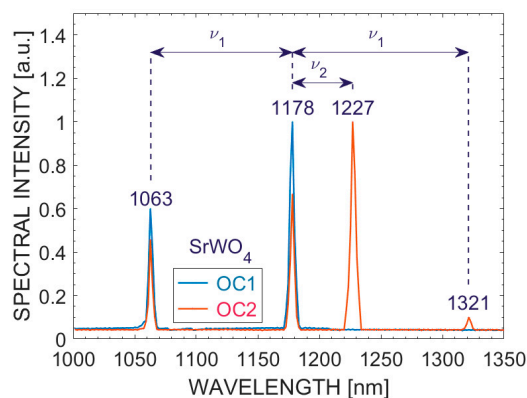

Figure 5. Output SRS radiation spectra for a long (3.6 cm) SrWO$_4$ crystal.

It can be seen that the only one short-shifted SRS radiation component was generated in the long SrWO$_4$ crystal (Figure 5), similarly as in the long BaWO$_4$ crystal (Figure 3a). It confirms that increasing the crystal length leads to the prevention of higher order short-shifted SRS component generation. It can be explained by a dispersion effect which is stronger in long media. And one more reason is a parametric coupling effect decreasing the oscillation threshold for higher order Stokes components in short crystals because the interaction length becomes lower than a coherence length of four-wave mixing of SRS components [30]. It is confirmed by generation of not only Stokes but also anti-Stokes ($\nu_1 - \nu_2$ and $2\nu_1 - \nu_2$) short-shifted SRS components in SrWO$_4$ (Figure 4). Short-shifted anti-Stokes generation can be explained only by four-wave mixing process of parametric coupling of two photons of the long-shifted Stokes component with one photon from the short-shifted Stokes component and one photon from the short-shifted anti-Stokes component. Similarly, short-shifted

second Stokes ($\nu_1 + 2\nu_2$) generation can be explained not only by cascade SRS but also by four-wave mixing process of parametric coupling of one photon from the (ν_1) long-shifted Stokes component with two photons from the first ($\nu_1 + \nu_2$) short-shifted Stokes component and one photon from the second ($\nu_1 + 2\nu_2$) Stokes component. For example, for $SrMoO_4$, using known Sellmeier equation [91], we can calculate wave mismatch of four-wave mixing generation of the ($\nu_1 + 2\nu_2$)-shifted Stokes component at 1256 nm (Table 3) by the formula [30]

$$\Delta k = (n_{S0} + n_{S2} - 2n_{S1}) \cdot 2\pi \lambda_{S1}^{-1} + (n_{S0} - n_{S2}) \cdot 2\pi \nu_2, \tag{15}$$

where n_{S0}, n_{S1} and n_{S2} are refractive indices at the Stokes components with the ν_1, ($\nu_1 + \nu_2$) and ($\nu_1 + 2\nu_2$) shifts, respectively, λ_{S1} is the wavelength of the ($\nu_1 + \nu_2$)-shifted Stokes component. We obtain $\Delta k \approx 4.8$ cm^{-1} corresponding to the coherence length [51] of $L_{coh} = \pi/\Delta k \approx 0.7$ cm which is substantially shorter than the $SrMoO_4$ crystal length of 1.7 cm, so we had no ($\nu_1 + 2\nu_2$)-shifted SRS generation at 1256 nm in the $SrMoO_4$ crystal (Figure 3b). On the contrary, the $SrWO_4$ crystal is shorter with a length of 1.4 cm being closer to the coherence length, so the ($\nu_1 + 2\nu_2$)-shifted SRS generation at 1279 nm took place (Figure 3c).

On the other hand, dispersion effect in long media leads to significant time delay between different SRS components preventing generation of higher order SRS components too. It is not so strong in short crystals (~1–4cm) in comparison with the fact that SRS generation at the cavity length detuning up to +50 μm leads to the time delay of the Stokes pulses relative to the pump pulse of about 0.6ps per round trip. The time delay between ($\nu_1 + \nu_2$)-shifted Stokes and (ν_1)-shifted Stokes components, due to dispersion in the $SrMoO_4$ crystal ($n_{1.063} = 1.8804$, $n_{1.173} = 1.8776$ and $n_{1.220} = 1.8766$ [86]), is only 0.06 ps at $L = 1.7$ cm per round trip. It can be comparable with the cavity length detuning time delay (0.6 ps) at 10-fold increase of the crystal length. So, in very long crystals such as the 8-cm long $BaWO_4$ [82], where the short-shifted ($\nu_1 + 2\nu_2$) second Stokes component and also the long-shifted ($2\nu_1$) second Stokes component were not generated (Figure 3a), the dispersion effect can be significant. But, as we believe, in shorter crystals such as the used $SrMoO_4$ and $SrWO_4$ crystals, the parametric coupling effect is predominant allowing the higher order short-shifted SRS generation in the shortest 1.4-cm $SrWO_4$ crystal. On other hand, dispersion in the $SrWO_4$ crystal with 2 times increased length of 3.6 cm also suppress it.

Figure 6 shows dependences of the output SRS pulse energy on the input pump pulse energy in the Raman lasers based on (a) the 1.7-cm long $SrMoO_4$ crystal [88] and (b) the 1.4-cm long $SrWO_4$ crystal at the output coupler OC1 for the case of perfect synchronization. In both the $SrMoO_4$ and $SrWO_4$ crystals, the single ν_1-shifted Stokes component was generated with the OC1. Slope efficiencies are comparable and amount of 17.3% and 15.2% in $SrMoO_4$ and $SrWO_4$, respectively. Output pulse energy reached 16 nJ and 13 nJ for the $SrMoO_4$ and $SrWO_4$ Raman lasers, respectively, at maximum pump pulse energy of 221 nJ. In the $SrMoO_4$ crystal with higher Raman gain, the SRS oscillation threshold was lower.

Let make estimations of the SRS oscillation threshold using expression (14) (we have $t_p = 500$ μs $\gg \tau_c = 6.7$ ns). The output coupler OC1 has reflectivity of $R_S = 87\%$ and 89% for the $SrMoO_4$ and $SrWO_4$ Raman lasers, respectively. The round-trip transmission of the intracavity medium (intracavity losses) can be estimated as $T_S \approx 98\%$ and the cavity losses increment can be estimated as $K = ln(1/T_S R_S) \approx 0.16$ and 0.14 for these lasers, respectively. Therefore, according to expression (14) at $p = 1$, we need to realize $G_{th} \approx 0.16$ and 0.14 for these lasers, respectively. Selecting the values of G_0, we find that the SRS gain increment G in expression (8) is equal to the threshold value of 0.16 or 0.14 at $G_{0th} \approx 0.44$ or 0.385 for the $SrMoO_4$ or $SrWO_4$ crystals, respectively. Numerical solution of the initial Equation (4) gives the same result. We also need to take into account strong focusing of the pump beam into the centre of the Raman-active crystal to the focal spot 35×30 μm^2 in area. An effective

length of SRS interaction L_{eff} for the strongly focused beam is lower than the Raman-active crystal length L. It can be determined [35] as

$$L_{eff} = 2z_R \arctan(L/2z_R), \tag{16}$$

where $z_R = \pi\, r_p^2 n / \lambda_p M^2$ is the Rayleigh length of a waist of the pump beam, r_p is the focal spot radius of the pump beam, n is the refractive index of the crystal. The effective interaction length L_{eff} should be used instead of L in the SRS oscillation threshold pump energy estimations. Due to Brewster incidence, we have an astigmatic beam in the crystal with the increased size of the beam in the horizontal axis (x) by a value of refractive index n. Thus, we have the focal spot radii of $r_{px} = 35 \cdot n$ µm and $r_{py} = 30$ µm in the crystal. Using the mean value of z_R, in expression (16), we obtain $L_{eff} \approx 1.5$ cm and 1.3 cm for the $SrMoO_4$ and $SrWO_4$ crystals, respectively. So, the threshold pump intensity should be about $I_{p,th} \approx G_{0th}/gL_{eff} \approx 52$ MW/cm^2 or 63 MW/cm^2 corresponding to the threshold pump pulse energy of about $I_{p,th}\tau_p\pi r_{px}r_{py} \approx 120$ nJ or 140 nJ for the $SrMoO_4$ or $SrWO_4$ Raman lasers, respectively. These calculations are in a good agreement with the experimental results (Figure 6).
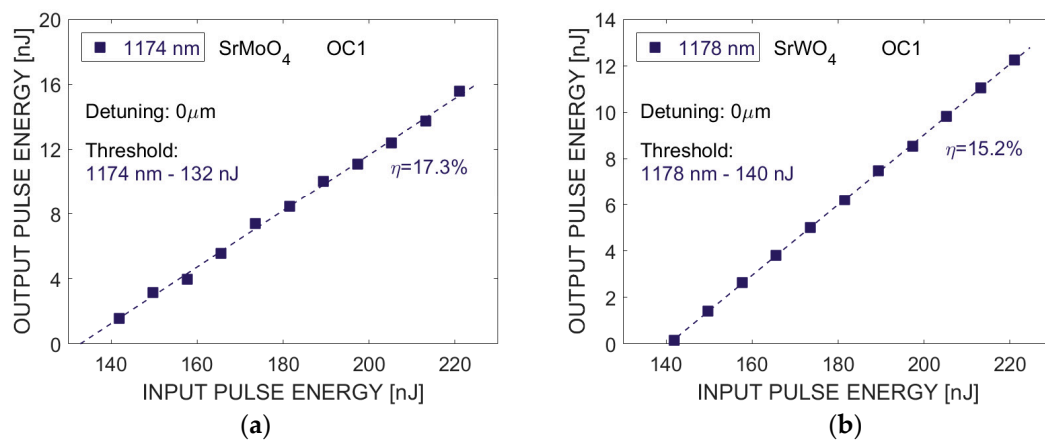

Figure 6. The output SRS pulse energy as a function of the input pump pulse energy in the (**a**) $SrMoO_4$ [88] and (**b**) $SrWO_4$ Raman lasers at the output coupler OC1 for the case of perfect synchronization.

Figure 7 shows dependences of output SRS pulse energy on the input pump pulse energy in the Raman lasers based on 1.7-cm long $SrMoO_4$ crystal [88] (Figure 7a) and 1.4-cm long $SrWO_4$ crystal (Figure 7b) with the output coupler OC2 for the case of perfect synchronization.
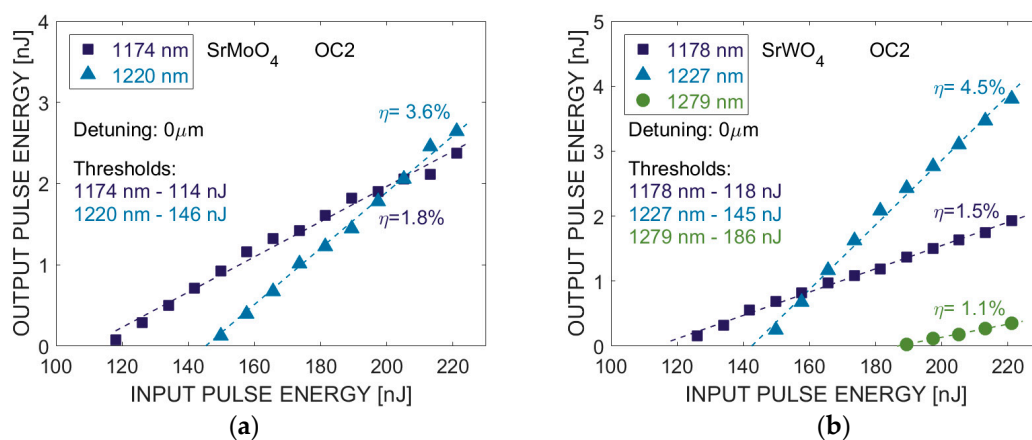

Figure 7. Dependences of the output SRS pulse energy on the input pump pulse energy in the (**a**) $SrMoO_4$ [88] and (**b**) $SrWO_4$ Raman lasers at the output coupler OC2 for the case of perfect synchronization.

As one can see, in contrast to the previous case, the output coupler OC2 allowed to achieve more efficient SRS operation of the $SrWO_4$ laser (7.1%, 6 nJ) than the $SrMoO_4$ laser (5.4%, 5 nJ) and it is also cascade-like with combined Raman shifts for the both. Note that the $SrWO_4$ Raman laser generation is more efficient because of higher efficiency of the secondary SRS conversion from the ν_1-shifted SRS component into the $(\nu_1 + \nu_2)$-shifted SRS component (4.5% against 3.6%). It can be explained by that the vibrational ν_2 Raman line is more intense in comparison with the ν_1 Raman line for $SrWO_4$ ($I_1 / I_2 = 3.5$, Table 1) than for $SrMoO_4$ ($I_1 / I_2 = 4.8$, Table 1). As a result, the $(\nu_1 + \nu_2)$-shifted SRS pulse energy (3.9 nJ at 1227 nm) in the $SrWO_4$ laser was 1.44 times higher than in the $SrMoO_4$ laser (2.7 nJ at 1220 nm). It even allowed to obtain the next cascade $(\nu_1 + 2\nu_2)$ of the short-shifted SRS conversion at 1279 nm with a pulse energy of 0.4 nJ in the $SrWO_4$ Raman laser (Figure 7b).

In order to achieve the strongest SRS pulse shortening, we realized the Raman laser cavity length detuning relative to the case of perfect synchronization (zero detuning). Figure 8 demonstrates the measured dependences of the output pulse energy (Figure 8a,b), the output pulse duration (Figure 8c,d) and output pulse peak power (Figure 8e,f) on the cavity length detuning for the $SrMoO_4$ (Figure 8a,c,e) and $SrWO_4$ (Figure 8b,d,f) lasers at OC2 under pumping with the maximal pulse energy of 221 nJ.

It can be seen from Figure 8a,b that SRS generation was observed only in a narrow range of the positive cavity length detuning from 0 up to +50 µm while the detuning range was essentially wider at the negative cavity length detuning (from 0 down to −220 µm). It is similar as in other synchronously pumped Raman lasers [65–78] and can be explained by non-efficient interaction between the pump and SRS pulses when only the leading edge of the SRS pulse is amplified at positive detuning. However, namely positive detuning (up to +50 µm) of the cavity length has allowed to obtain the strongest SRS pulse shortening, as can be seen from Figure 8c,d.

It is necessary to note that the $(\nu_1 + \nu_2)$-shifted (at 1220 or 1227 nm in the $SrMoO_4$ or $SrWO_4$ laser) and $(\nu_1 + 2\nu_2)$-shifted (at 1279 nm in the $SrWO_4$ laser) Stokes pulses had strong self-shortening in the whole range of cavity length detuning and did not exceed 7 ps at negative and zero detuning of the cavity length. It had the strongest pulse shortening down to about 1.4 ps at the cavity length positive detuning of +50 µm in both Raman lasers (Figure 8c,d). The shortest pulse durations of 1.46 ps and 1.41 ps for the $SrMoO_4$ and $SrWO_4$ lasers, respectively, were close to the limit given by the inverse width of the widest ν_2 vibrational line ($1/\pi c\Delta\nu_2 = 1.0$ ps and 1.2 ps for $SrMoO_4$ and $SrWO_4$, respectively). This extreme pulse shortening can be explained by the theory of ultra-short SRS pulse formation at intracavity pumping [62] taking into account that generation of the highly shortened $(\nu_1 + \nu_2)$-shifted or $(\nu_1 + 2\nu_2)$-shifted SRS pulses in our extracavity Raman lasers were intracavity pumped by the ν_1-shifted or $(\nu_1 + \nu_2)$-shifted SRS radiation.

The values of peak power were significantly influenced by the pulse shortening. As it can be seen in Figure 8e,f, the position of the maximum peak power at the 1220 nm for $SrMoO_4$ [88] and at 1227 nm for $SrWO_4$ has a shift from the zero detuning due to strong pulse shortening. While the output pulse energy maximum of the $(\nu_1 + \nu_2)$-shifted SRS component was obtained for the zero detuning (Figure 8a,b) but the peak power of its component reached the maximum value for detuning of +20 µm (Figure 8e,f) in both the lasers. For this setup, the peak power levels of 500 W and 650 W were achieved in the $SrMoO_4$ and $SrWO_4$ lasers, respectively. It is higher than the peak power of the ν_1-shifted SRS component generated not only at the OC2 but also at the OC1 in the both Raman lasers.
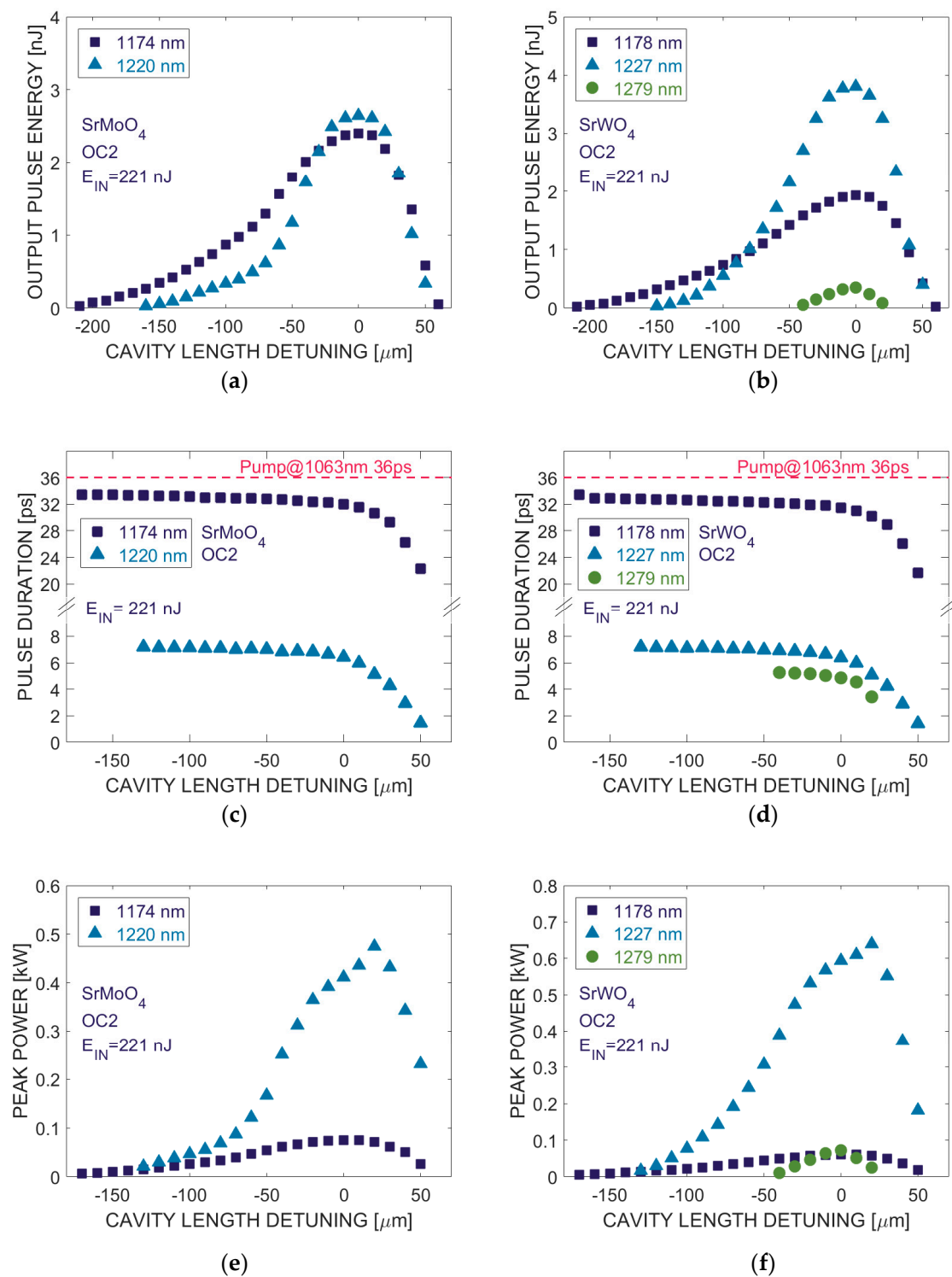
Figure 8. The dependences of the output pulse energy (**a**,**b**), the output pulse duration (**c**,**d**) and the output pulse peak power (**e**,**f**) on the cavity length detuning for the SrMoO$_4$ [88] (**a**,**c**,**e**) and SrWO$_4$ (**b**,**d**,**f**) lasers at OC2 under pumping with the maximal pulse energy of 221 nJ.

6. Conclusions

In this paper, we have presented a comparative investigation of characteristics of spontaneous and stimulated Raman scattering in different alkali-earth tungstate and molybdate crystals at both high (ν_1) and low (ν_2) wavenumber anionic group vibrations. It was found that, among these crystals,

$SrMoO_4$ and $SrWO_4$ crystals are the most perspective for SRS generation on both the stretching and bending modes of internal anionic group vibrations with the strongest SRS pulse shortening under synchronous laser pumping. It is caused by the fact that they have not only highly intense stretching mode ν_1 Raman line for efficient primary extracavity long-shifted SRS conversion but also the widest bending mode ν_2 Raman line for the strongest SRS pulse shortening down to the inverse width of the widest Raman line at the secondary intracavity short-shifted SRS conversion. The possibilities of the strongest 26-fold pulse shortening down to 1.4 ps at the Stokes component with the combined $(\nu_1 + \nu_2)$ Raman shift of the synchronously pumped extracavity Raman lasers based on $SrMoO_4$ and $SrWO_4$ crystals have been demonstrated. This value of 1.4 ps is close to the inverse width of the widest ν_2 Raman line ($1/\pi c \Delta\nu_2 \approx 1$ ps). It was found that synchronously pumped cascade SRS with combined $(\nu_1 + \nu_2)$ Raman shift is more efficient in the $SrWO_4$ crystal because the vibrational ν_2 Raman line is more intensive in comparison with the vibrational ν_1 Raman line for $SrWO_4$ than for $SrMoO_4$. It was also found that the high order Stokes and anti-Stokes short-shifted SRS generation under extracavity synchronous pumping can be reached using the crystals with a short length (~1 cm) in comparison with a coherence length of parametric Raman interaction of the long-shifted and short-shifted SRS components but in long crystals (>3 cm), the higher-order short-shifted and long-shifted SRS generation is suppressed due to a dispersion effect.

Author Contributions: Conceptualization, S.N.S.; Formal analysis, M.F. and S.N.S.; Investigation, M.F., S.N.S., M.J., D.V., V.E.S., L.I.I., E.E.D. and I.S.V.; Methodology, M.F. and S.N.S.; Resources, V.E.S., L.I., E.E.D. and I.S.V.; Supervision, P.G.Z. and V.K.; Validation, P.G.Z. and V.K.; Visualization, M.F.; Writing—original draft, M.F. and S.N.S.; Writing—review & editing, M.F., S.N.S., M.J., D.V., P.G.Z. and V.K.

Conflicts of Interest: The authors declare no conflict of interest.

References

1. Basiev, T.T.; Sobol, A.A.; Zverev, P.G.; Osiko, V.V.; Powell, R.C. Comparative spontaneous Raman spectroscopy of crystals for Raman lasers. *Appl. Opt.* **1999**, *38*, 594–598. [CrossRef] [PubMed]
2. Basiev, T.T.; Sobol, A.A.; Zverev, P.G.; Ivleva, L.I.; Osiko, V.V.; Powell, R.C. Raman spectroscopy of crystals for stimulated Raman scattering. *Opt. Mater.* **1999**, *11*, 307–314. [CrossRef]
3. Basiev, T.T.; Sobol, A.A.; Voronko, Y.K.; Zverev, P.G. Spontaneous Raman spectroscopy of tungstate and molybdate crystals for Raman lasers. *Opt. Mater.* **2000**, *15*, 205–216. [CrossRef]
4. Kaminskii, A.A.; Eichler, H.J.; Ueda, K.I.; Klasson, N.V.; Redkin, B.S.; Li, L.E.; Findeisen, J.; Jaque, D.; Garcia-Sole, J.; Fernandez, J.; et al. Properties of Nd^{3+}-doped and undoped $PbWO_4$, $NaY(WO_4)_2$, $CaWO_4$ as laser-active and stimulated Raman scattering-active crystals. *Appl. Opt.* **1999**, *38*, 4533–4547. [CrossRef]
5. Zverev, P.G.; Basiev, T.T.; Sobol, A.A.; Skornvakov, V.V.; Ivleva, L.I.; Polozkov, N.M.; Osiko, V.V. Stimulated Raman scattering in alkaline-earth tungstate crystals. *Quantum Electron.* **2000**, *30*, 55–59. [CrossRef]
6. Černý, P.; Zverev, P.G.; Jelínková, H.; Basiev, T.T. Efficient Raman shifting of picosecond pulses using $BaWO_4$ crystal. *Opt. Commun.* **2000**, *177*, 397–404. [CrossRef]
7. Černý, P.; Jelínková, H.; Basiev, T.T.; Zverev, P.G. Properties of transient and steady-state stimulated Raman scattering in $KGd(WO_4)_2$ and $BaWO_4$ tungstate crystals. *Proc. SPIE* **2001**, *4268*, 101–108.
8. Zverev, P.G.; Basiev, T.T.; Ivleva, L.I.; Osiko, V.V.; Polozkov, N.M. Raman laser on strontium tungstate crystal. *OSA TOPS* **2002**, *68*, 70–73.
9. Zverev, P.G.; Karasik, A.Y.; Basiev, T.T.; Ivleva, L.I.; Osiko, V.V. Stimulated Raman scattering of picosecond pulses in $SrMoO_4$ and $Ca_3(VO_4)_2$ crystals. *Quantum Electron.* **2003**, *33*, 331–334. [CrossRef]
10. Černý, P.; Jelínková, H.; Zverev, P.G.; Basiev, T.T. Solid state lasers with Raman frequency conversion. *Prog. Quantum Electron.* **2004**, *28*, 113–143. [CrossRef]
11. Basiev, T.T.; Zverev, P.G.; Karasik, A.Y.; Osiko, V.V.; Sobol, A.A.; Chunaev, D.S. Picosecond stimulated Raman scattering in crystals. *JETP* **2004**, *99*, 934–941. [CrossRef]

12. Basiev, T.T.; Gavrilov, A.V.; Osiko, V.V.; Smetanin, S.N.; Fedin, A.V. High-average-power SRS conversion of radiation in a BaWO$_4$ crystal. *Quantum Electron.* **2004**, *34*, 649–651. [CrossRef]

13. Basiev, T.T.; Danileiko, Y.K.; Doroshenko, M.E.; Fedin, A.V.; Gavrilov, A.V.; Osiko, V.V.; Smetanin, S.N. High-energy BaWO$_4$ Raman laser pumped by a self-phase-conjugated Nd:GGG laser. *Laser Phys.* **2004**, *14*, 917–921.

14. Basiev, T.T.; Doroshenko, M.E.; Osiko, V.V.; Sverchkov, S.E.; Galagan, B.I. New mid IR (1.5–22 μm) Raman lasers based on barium tungstate and barium nitrate crystals. *Laser Phys. Lett.* **2005**, *2*, 237–238. [CrossRef]

15. Chen, Y.F.; Su, K.W.; Zhang, H.J.; Wang, J.Y.; Jiang, M.H. New mid IR (1.5–22 μm) Efficient diode-pumped actively Q-switched Nd:YAG/BaWO$_4$ intracavity Raman laser. *Opt. Lett.* **2005**, *30*, 3335–3337. [CrossRef]

16. Basiev, T.T.; Basieva, M.N.; Doroshenko, M.E.; Fedorov, V.V.; Osiko, V.V.; Mirov, S.B. Stimulated Raman scattering in mid IR spectral range 2.31–2.75–3.7 μm in BaWO$_4$ crystal under 1.9 and 1.56 μm pumping. *Laser Phys. Lett.* **2006**, *3*, 17–20. [CrossRef]

17. Ding, S.; Zhang, X.; Wang, Q.; Su, F.; Li, S.; Fan, S.; Liu, Z.; Chang, J.; Zhang, S.; Wang, S.; et al. Highly efficient Raman frequency converter with strontium tungstate crystal. *IEEE J. Quantum Electron.* **2006**, *42*, 78–84. [CrossRef]

18. Li, S.; Zhang, X.; Wang, Q.; Zhang, X.; Cong, Z.; Zhang, H.; Wang, J. Diode-side-pumped intracavity frequency-doubled Nd:YAG/BaWO$_4$ Raman laser generating average output power of 3.14 W at 590 nm. *Opt. Lett.* **2007**, *32*, 2951–2953. [CrossRef]

19. Fan, Y.X.; Liu, Y.; Wang, Q.; Fan, L.; Wang, H.T.; Jia, G.H.; Tu, C.Y. High-efficiency eye-safe intracavity Raman laser at 1531 nm with SrWO$_4$ crystal. *Appl. Phys. B* **2008**, *93*, 327–330. [CrossRef]

20. Zong, N.; Cui, Q.J.; Ma, Q.L.; Zhang, X.F.; Lu, Y.F.; Li, C.M.; Cui, D.F.; Xu, Z.Y.; Zhang, H.J.; Wang, J.Y. High average power 1.5 μm eye-safe Raman shifting in BaWO$_4$ crystals. *Appl. Opt.* **2009**, *48*, 7–10. [CrossRef]

21. Fan, L.; Fan, Y.X.; Li, Y.Q.; Zhang, H.; Wang, Q.; Wang, J.; Wang, H.T. High-efficiency continuous-wave Raman conversion with a BaWO$_4$ Raman crystal. *Opt. Lett.* **2009**, *34*, 1687–1689. [CrossRef] [PubMed]

22. Fan, L.; Fan, Y.X.; Duan, Y.H.; Wang, Q.; Wang, H.T.; Jia, G.H.; Tu, C.Y. Continuous-wave intracavity Raman laser at 1179.5 nm with SrWO$_4$ Raman crystal in diode-end-pumped Nd:YVO$_4$ laser. *Appl. Phys. B* **2009**, *94*, 553–557. [CrossRef]

23. Basiev, T.T.; Basieva, M.N.; Gavrilov, A.V.; Ershkov, M.N.; Ivleva, L.I.; Osiko, V.V.; Smetanin, S.N.; Fedin, A.V. Efficient conversion of Nd:YAG laser radiation to the eye-safe spectral region by stimulated Raman scattering in BaWO$_4$ crystal. *Quantum Electron.* **2010**, *40*, 710–715. [CrossRef]

24. Lee, A.J.; Pask, H.M.; Piper, J.A.; Zhang, H.; Wang, J. An intracavity, frequency-doubled BaWO$_4$ Raman laser generating multi-watt continuous-wave, yellow emission. *Opt. Express* **2010**, *18*, 5984–5992. [CrossRef] [PubMed]

25. Yu, H.; Li, Z.; Lee, A.J.; Li, J.; Zhang, H.; Wang, J.; Pask, H.M.; Piper, J.A.; Jiang, M. A continuous wave SrMoO$_4$ Raman laser. *Opt. Lett.* **2011**, *36*, 579–581. [CrossRef] [PubMed]

26. Shen, H.; Wang, Q.; Zhang, X.; Liu, Z.; Bai, F.; Chan, X.; Cong, Z.; Gao, L.; Wu, Z.; Wang, W.; et al. Simultaneous dual-wavelength generation at 1502 and 1527 nm in ceramic neodymium-doped yttrium aluminum garnet/BaWO$_4$ Raman laser. *Appl. Phys. Express* **2012**, *5*, 112704. [CrossRef]

27. Lan, R.; Ding, S.; Wang, M.; Zhang, J. A compact passively Q-switched SrWO$_4$ Raman laser with mode-locked modulation. *Laser Phys. Lett.* **2013**, *10*, 025801. [CrossRef]

28. Basiev, T.T.; Doroshenko, M.E.; Ivleva, L.I.; Smetanin, S.N.; Jelínek, M.; Kubeček, V.; Jelínková, H. Four-wave-mixing generation of SRS components in BaWO$_4$ and SrWO$_4$ crystals under picosecond excitation. *Quantum Electron.* **2013**, *43*, 616–620. [CrossRef]

29. Zhao, J.; Zhang, X.; Guo, X.; Bao, X.; Li, L.; Gui, J. Diode-pumped actively Q-switched Tm, Ho:GdVO$_4$/BaWO$_4$ intracavity Raman laser at 2533 nm. *Opt. Lett.* **2013**, *38*, 1206–1208. [CrossRef]

30. Smetanin, S.N.; Doroshenko, M.E.; Ivleva, L.I.; Jelínek, M.; Kubeček, V.; Jelínková, H. Low-threshold parametric Raman generation of high-order Raman components in crystals. *Appl. Phys. B* **2014**, *117*, 225–234. [CrossRef]

31. Zhang, H.N.; Chen, X.H.; Wang, Q.P.; Zhang, X.Y.; Chang, J.; Gao, L.; Shen, H.B.; Cong, Z.H.; Liu, Z.J. High-efficiency diode-pumped actively Q-switched ceramic Nd:YAG/BaWO$_4$ Raman laser operating at 1666 nm. *Opt. Lett.* **2014**, *39*, 2649–2651. [CrossRef] [PubMed]

32. Kuzucu, O. Watt-level, mid-infrared output from a BaWO$_4$ external-cavity Raman laser at 2.6 μm. *Opt. Lett.* **2015**, *40*, 5078–5081. [CrossRef] [PubMed]

33. Men, S.; Liu, Z.; Cong, Z.; Liu, Y.; Xia, J.; Zhang, S.; Cheng, W.; Li, Y.; Tu, C.; Zhang, X. Single-frequency $CaWO_4$ Raman amplifier at 1178 nm. *Opt. Lett.* **2015**, *40*, 530–533. [CrossRef]

34. Zhao, J.; Li, Y.; Zhang, S.; Li, L.; Zhang, X. Diode-pumped actively Q-switched $Tm:YAP/BaWO_4$ intracavity Raman laser. *Opt. Express* **2015**, *23*, 10075–10080. [CrossRef] [PubMed]

35. Farinello, P.; Pirzio, F.; Zhang, X.; Petrov, V. Efficient picosecond traveling-wave Raman conversion in a $SrWO_4$ crystal pumped by multi-Watt MOPA lasers at 1064 nm. *Appl. Phys. B* **2015**, *120*, 731–735. [CrossRef]

36. Zhang, H.; Li, P. High-efficiency eye-safe $Nd:YAG/SrWO_4$ Raman laser operating at 1664 nm. *Appl. Phys. B* **2016**, *122*, 12. [CrossRef]

37. Sheng, Q.; Lee, A.; Spence, D.; Pask, H. Wavelength tuning and power enhancement of an intracavity $Nd:GdVO_4$-$BaWO_4$ Raman laser. *Opt. Express* **2018**, *26*, 32145–32155. [CrossRef] [PubMed]

38. Liu, Z.; Men, S.; Cong, Z.; Qin, Z.; Zhang, X.; Zhang, H. A pulsed single-frequency $Nd:GGG/BaWO_4$ Raman laser. *Laser Phys.* **2018**, *28*, 045002. [CrossRef]

39. Kaminskii, A.A.; Bagaev, S.N.; Ueda, K.; Takaichi, K.; Eichler, H.J. High-order picosecond SRS and self-SRS generation in Nd^{3+}-doped $CaMoO_4$, $SrMoO_4$ and $SrWO_4$ laser crystals. *Cryst. Rep.* **2012**, *47*, 653–657. [CrossRef]

40. Voronina, I.S.; Ivleva, L.I.; Basiev, T.T.; Zverev, P.G.; Polozkov, N.M. Active Raman media: $SrWO_4:Nd^{3+}$, $BaWO_4:Nd^{3+}$. Growth and characterization. *J. Optoelectron. Adv. Mater.* **2003**, *5*, 887–892.

41. Ivleva, L.I.; Basiev, T.T.; Voronina, I.S.; Zverev, P.G.; Osiko, V.V.; Polozkov, N.M. $SrWO_4:Nd^{3+}$—New material for multifunctional lasers. *Opt. Mater.* **2003**, *23*, 439–442. [CrossRef]

42. Brenier, A.; Jia, G.; Tu, C. Raman lasers at 1.171 and 1.517 μm with self-frequency conversion in $SrWO_4:Nd^{3+}$ crystal. *J. Phys. Condens. Matter* **2004**, *16*, 9103–9108. [CrossRef]

43. Jelínková, H.; Šulc, J.; Basiev, T.T.; Zverev, P.G.; Kravtsov, S.V. Stimulated Raman scattering in $Nd:SrWO_4$. *Laser Phys. Lett.* **2005**, *2*, 4–11. [CrossRef]

44. Jia, G.; Tu, C.; Brenier, A.; You, Z.; Li, J.; Zhu, Z.; Wang, Y.; Wu, B. Thermal and optical properties of $Nd^{3+}:SrWO_4$: A potential candidate for eye-safe 1.517 μm Raman lasers. *Appl. Phys. B* **2005**, *87*, 627–632. [CrossRef]

45. Šulc, J.; Jelínková, H.; Basiev, T.T.; Doroshenko, M.E.; Ivleva, L.I.; Osiko, V.V.; Zverev, P.G. $Nd:SrWO_4$ and $Nd:BaWO_4$ Raman lasers. *Opt. Mater.* **2007**, *30*, 195–197. [CrossRef]

46. Doroshenko, M.E.; Basiev, T.T.; Vassilev, S.V.; Komar, V.K.; Kosmyna, M.B.; Šulc, J.; Jelínková, H. Comparative study of lasing properties of self-Raman capable tungstate and molybdate crystals doped with Nd^{3+} ions under diode pumping. *Opt. Mater.* **2007**, *30*, 54–57. [CrossRef]

47. Basiev, T.T.; Doroshenko, M.E.; Ivleva, L.I.; Voronina, I.; Konjushkin, V.; Osiko, V.V.; Vassilev, S.V. Demonstration of high self-Raman laser performance of a diode-pumped $SrMoO_4:Nd^{3+}$ crystal. *Opt. Lett.* **2009**, *34*, 1102–1104. [CrossRef]

48. Lupei, A.; Achim, A.; Lupei, V.; Gheorghe, C.; Gheorghe, L.; Hau, S. RE^{3+} doped $SrWO_4$ as laser and nonlinear active crystals. *Rom. J. Phys.* **2009**, *54*, 919–928.

49. Basiev, T.T.; Smetanin, S.N.; Fedin, A.V.; Shurygin, A.S. Intracavity SRS conversion in diode-pumped multifunctional $Nd^{3+}:SrMoO_4$ laser crystal. *Quantum Electron.* **2010**, *40*, 704–709. [CrossRef]

50. Dunaeva, E.E.; Ivleva, L.I.; Doroshenko, M.E.; Zverev, P.G.; Nekhoroshikh, A.N.; Osiko, V.V. Synthesis, characterization, spectroscopy and laser operation of $SrMoO_4$ crystals co-doped with Tm^{3+} and Ho^{3+}. *J. Cryst. Growth* **2015**, *432*, 1–5. [CrossRef]

51. Smetanin, S.N.; Jelínek, M.; Kubeček, V.; Jelínková, H.; Ivleva, L.I.; Shurygin, A.S. Four-wave-mixing and nonlinear cavity dumping of 280 picosecond 2nd Stokes pulse at 1.3 μm from $Nd:SrMoO_4$ self-Raman laser. *Laser Phys. Lett.* **2016**, *13*, 015801. [CrossRef]

52. Smetanin, S.N.; Jelínek, M.; Kubeček, V.; Jelínková, H.; Ivleva, L.I. Parametric second Stokes Raman laser output pulse shortening to 300 ps due to depletion of pumping of intracavity Raman conversion. *Appl. Phys. B* **2016**, *122*, 260. [CrossRef]

53. Jelínek, M.; Kubeček, V.; Ivleva, L.I.; Smetanin, S.N. Eye-safe, diode-pumped, passively Q-switched, self-Raman $Nd:SrMoO_4$ laser generating at ${}^4F_{3/2} - > {}^4I_{13/2}$ transition. In *Laser Congress (ASSL, LAC)*; Paper JTu2A.17; OSA Technical Digest Series; OSA: Denver, CO, USA, 2017.

54. Lubeigt, W.; Bonner, G.M.; Hastie, J.E.; Dawson, M.D.; Burns, D.; Kemp, A.J. Continuous-wave diamond Raman laser. *Opt. Lett.* **2010**, *35*, 2994–2996. [CrossRef] [PubMed]

55. Savitski, V.G.; Friel, I.; Hastie, J.E.; Dawson, M.D.; Burns, D.; Kemp, A.J. Characterization of single-crystal synthetic diamond for multi-watt continuous-wave Raman lasers. *IEEE J. Quantum Electron.* **2012**, *48*, 328–337. [CrossRef]

56. Eremenko, A.S.; Karpuhkin, S.N.; Stepanov, A.I. Stimulated Raman scattering of the second harmonic of a neodymium laser in nitrate crystals. *Sov. L. Quantum Electron.* **1980**, *10*, 113–114. [CrossRef]

57. Murray, J.T.; Powell, R.C.; Peyghambarian, N.; Smith, D.; Austin, W.; Stolzenberger, R.A. Generation of 1.5-μm radiation through intracavity solid-state Raman shifting in $Ba(NO_3)_2$ nonlinear crystals. *Opt. Lett.* **1995**, *20*, 1017–1019. [CrossRef] [PubMed]

58. Porto, S.P.S.; Scott, J.F. Raman spectra of $CaWO_4$, $SrWO_4$, $CaMoO_4$, and $SrMoO_4$. *Phys. Rev.* **1967**, *157*, 716–719. [CrossRef]

59. Zverev, P.G.; Basiev, T.T.; Sobol, A.A.; Ermakov, I.V.; Gellerman, W. $BaWO_4$ crystal for quasi-cw yellow Raman laser. *OSA TOPS* **2001**, *50*, 212–217.

60. Graham, K.; Fedorov, V.V.; Mirov, S.B.; Doroshenko, M.E.; Basiev, T.T.; Orlovskii, Y.V.; Osiko, V.V.; Badikov, V.; Panyutin, V.L. Pulsed mid-IR Cr^{2+}:ZnS and Cr^{2+}:ZnSe lasers pumped by Raman-shifted Q-switched neodymium lasers. *Quantum Electron.* **2004**, *34*, 8–14. [CrossRef]

61. Sun, W.J.; Wang, Q.P.; Liu, Z.J.; Zhang, X.Y.; Wang, G.T.; Bai, F.; Lan, W.X.; Wan, X.B.; Zhang, H.J. An efficient 1103 nm $Nd:YAG/BaWO_4$ Raman laser. *Laser Phys. Lett.* **2011**, *8*, 512–515. [CrossRef]

62. Li, L.; Zhang, X.; Liu, Z.; Wang, Q.; Cong, Z.; Zhang, Y.; Wang, W.; Wu, Z.; Zhang, H. A high-power diode-side-pumped $Nd:YAG/BaWO_4$ Raman laser at 1103 nm. *Laser Phys. Lett.* **2013**, *23*, 045402. [CrossRef]

63. Li, X.; Lee, A.J.; Huo, Y.; Zhang, H.; Wang, J.; Piper, J.A.; Pask, H.M.; Spence, D.J. Managing SRS competition in a miniature visible $Nd:YVO_4/BaWO_4$ Raman laser. *Opt. Express* **2012**, *20*, 19305–19312. [CrossRef] [PubMed]

64. Shen, H.; Wang, Q.; Zhang, X.; Chen, X.; Cong, Z.; Wu, Z.; Bai, F.; Lan, W.; Gao, L. 1st-Stokes and 2nd-Stokes dual-wavelength operation and mode-locking modulation in diode-side-pumped $Nd:YAG/BaWO_4$ Raman laser. *Opt. Express* **2012**, *20*, 17823–17832. [CrossRef] [PubMed]

65. Carmen, R.L.; Shimizu, F.; Wang, C.S.; Bloembergen, N. Theory of Stokes pulse shapes in transient stimulated Raman scattering. *Phys. Rev. A* **1970**, *2*, 60–72. [CrossRef]

66. Isaev, S.K.; Kornienko, L.S.; Kravtsov, N.V.; Serkin, V.N. Formation of ultrashort light pulses in a laser with a bleachable filter by intracavity generation of Raman emission. *Sov. J. Quantum Electron.* **1981**, *11*, 365–370. [CrossRef]

67. Chunaev, D.S.; Basiev, T.T.; Konushkin, V.A.; Papashvili, A.G.; Karasik, A.Y. Synchronously pumped intracavity YLF-Nd-KGW picosecond Raman lasers and $LiF:F_2^-$ amplifiers. *Laser Phys. Lett.* **2008**, *5*, 589–592. [CrossRef]

68. Weitz, M.; Theobald, C.; Wallenstein, R.; L'huillier, J.A. Passively mode-locked picosecond $Nd:YVO_4$ self-Raman laser. *Appl. Phys. Lett.* **2008**, *92*, 091122. [CrossRef]

69. Grigoryanand, G.G.; Sogomonyan, S.B. Synchronously pumped picosecond Raman laser utilizing an $LiIO_3$ crystal. *Sov. J. Quantum Electron.* **1989**, *19*, 1402–1404. [CrossRef]

70. Grenados, E.; Spence, D.J. Pulse compression in synchronously pumped mode locked Raman lasers. *Sov. Opt. Express* **2010**, *18*, 20422–20427. [CrossRef]

71. Warrier, A.M.; Lin, J.; Pask, H.M.; Mildren, R.P.; Coutts, D.W.; Spence, D.J. Highly efficient picosecond diamond Raman laser at 1240 and 1485 nm. *Opt. Express* **2014**, *22*, 3325–3333. [CrossRef] [PubMed]

72. Murtagh, M.; Lin, J.; Mildren, R.P.; Spence, D.J. Ti:sapphire-pumped diamond Raman laser with sub-100-fs pulse duration. *Opt. Lett.* **2014**, *39*, 2975–2978. [CrossRef] [PubMed]

73. Murtagh, M.; Lin, J.; Mildren, R.P.; McConnell, G.; Spence, D.J. Efficient diamond Raman laser generating 65 fs pulses. *Opt. Express* **2015**, *23*, 15504–15513. [CrossRef] [PubMed]

74. Lin, J.; Spence, D.J. 25.5 fs dissipative soliton diamond Raman laser. *Opt. Lett.* **2016**, *41*, 1861–1864. [CrossRef]

75. Murtagh, M.; Lin, J.; Trägårdh, J.; McConnell, G.; Spence, D.J. Ultrafast second-Stokes diamond Raman laser. *Opt. Express* **2016**, *24*, 8149–8155. [CrossRef] [PubMed]

76. Perillo, E.P.; Jarrett, J.W.; Liu, Y.L.; Hassan, A.; Fernée, D.C.; Goldak, J.R.; Bonteanu, A.; Spence, D.J.; Yen, H.C.; Dunn, A.K. Two-color multiphoton *in vivo* imaging with a femtosecond diamond Raman laser. *Light Sci. Appl.* **2017**, *6*, e17095. [CrossRef] [PubMed]

77. Grenados, E.; Pask, H.M.; Spence, D.J. Synchronously pumped continuous-wave mode-locked yellow Raman laser at 559 nm. *Opt. Express* **2009**, *17*, 569–574. [CrossRef]

78. Grenados, E.; Pask, H.M.; Esposito, E.; McConnell, G.; Spence, D.J. Multi-wavelength, all-solid-state, continuous wave mode locked picosecond Raman laser. *Opt. Express* **2010**, *18*, 5289–5294. [CrossRef] [PubMed]

79. Gao, X.; Long, M.; Chen, M. Study on picosecond collinear eight Stokes Raman laser generation. *Appl. Opt.* **2017**, *56*, 1383–1387. [CrossRef]

80. Warrier, A.M.; Lin, J.; Pask, H.M.; Lee, A.J.; Spence, D.J. Multiwavelength ultrafast LiNbO$_3$ Raman laser. *Opt. Express* **2015**, *23*, 25582–25587. [CrossRef]

81. Frank, M.; Jelínek, M.; Vyhlídal, D.; Kubeček, V.; Ivleva, L.I.; Zverev, P.G.; Smetanin, S.N. Multi-wavelength picosecond BaWO$_4$ Raman laser with long and short Raman shifts and 12-fold pulse shortening down to 3 ps at 1227 nm. *Laser Phys.* **2018**, *28*, 025403. [CrossRef]

82. Frank, M.; Smetanin, S.N.; Jelínek, M.; Vyhlídal, D.; Ivleva, L.I.; Zverev, P.G.; Kubeček, V. Highly efficient picosecond all-solid-state Raman laser at 1179 and 1227 nm on single and combined Raman lines in a BaWO$_4$ crystal. *Opt. Lett.* **2018**, *43*, 2527–2530. [CrossRef] [PubMed]

83. Akhmanov, S.A.; Drabovich, K.N.; Sukhorukov, A.P.; Chirkin, A.S. Stimulated Raman scattering in a field of ultrashort light pulses. *Sov. Phys. JETP* **1971**, *32*, 266–273.

84. Duncan, M.D.; Mahon, R.; Tankersley, L.L.; Reintjes, J. Transient stimulated Raman amplification in hydrogen. *J. Opt. Soc. Am. B* **1988**, *5*, 37–52. [CrossRef]

85. Smetanin, S.N. Determination of the stimulated Raman scattering threshold for a pump pulse of arbitrary width. *Opt. Spectrosc.* **2016**, *121*, 395–404. [CrossRef]

86. Penzkofer, A.; Laubereau, A.; Kaiser, W. High intensity Raman interactions. *Prog. Quant. Electron.* **2016**, *6*, 55–140. [CrossRef]

87. Lisinetskii, V.A.; Bus'ko, D.N.; Chulkov, R.V.; Grabchikov, A.S.; Apanasevich, P.A.; Orlovich, V.A. Low-threshold lasing in stimulated Raman lasers with nanosecond pumping. *J. Appl. Spect.* **2008**, *75*, 300–307. [CrossRef]

88. Frank, M.; Smetanin, S.N.; Jelínek, M.; Vyhlídal, D.; Kopalkin, A.A.; Shukshin, V.E.; Ivleva, L.I.; Zverev, P.G.; Kubeček, V. Synchronously-pumped all-solid-state SrMoO4 Raman laser generating at combined vibrational Raman modes with 26-fold pulse shortening down to 1.4 ps at 1220 nm. *J. Opt. Laser Technol.* **2019**, *111*, 129–133. [CrossRef]

89. Frank, M.; Jelínek, M.; Vyhlídal, D.; Kubeček, V. Optimization of passively mode-locked Nd:GdVO$_4$ laser with the selectable pulse duration 15–70 ps. *Proc. SPIE* **2016**, *10142*, 101421E.

90. Bespalov, V.I.; Pasmanic, G.A. Stimulated Mandel'shtam-Brillouin and stimulated entropy backscattering of light pulses. *Sov. Phys. J. Exp. Theor. Phys.* **1970**, *31*, 168–174.

91. *Handbook of Optics. Volume IV: Optical Properties of Materials, Nonlinear Optics, Quantum Optics*, 3rd ed.; The McGraw-Hill Companies, Inc.: New York, NY, USA, 2010.